Hydrothermally engineered *Eriobotrya japonica leaves*/MgO nanocomposites with potential applications in wastewater treatment

Noureddine El Messaoudi [a] *, Mohammed El Khomri [a], Yasmine Fernine [b], Amal Bouich [c], Abdellah Lacherai [a], Amane Jada [d], Farooq Sher [e], Eder C. Lima [f]

[a] *Laboratory of Applied Chemistry and Environment, Ibn Zohr University, Agadir 80000, Morocco*

[b] *Engineering Laboratory of Organometallic, Molecular Materials and Environment, Sidi Mohamed Ben Abdellah University, Fez 30000, Morocco*

[c] *Department of Applied Physics, Institute of Design and Manufacturing (IDF), Polytechnic University of Valencia, Valencia 46000, Spain*

[d] *Institute of Materials Science of Mulhouse (IS2M), High Alsace University, Mulhouse 68100, France*

[e] *Department of Engineering, School of Science and Technology, Nottingham Trent University, Nottingham NG11 8NS, United Kingdom*

[f] *Institute of Chemistry, The Federal University of Rio Grande do Sul (UFRGS), Porto Alegre-RS 91501-970, Brazil*

*Corresponding author. Tel.: +212675233867

E-mail address: noureddine.elmessaoudi@edu.uiz.ac.ma (N. El Messaoudi)

Abstract

The hydrothermal method as the eco-friendly environmental method was used in this study to prepare a high efficient nanocomposite adsorbent based on the biochar (BC) derived from *Eriobotrya japonica* leaves and magnesium oxide nanoparticles (MgO NPs). The prepared materials were characterized using FTIR, BET, SEM-EDX, TEM, and XRD. The adsorption of tartrazine (TZ) on BC, MgO NPs, and BC@MgO NPs was better described by the kinetic pseudo 2nd order model and followed the Langmuir isotherm model. The maximum uptake (*Qm)* was 643.50 mg g^{-1} at 25±1 °C for BC@MgO NPs. The calculated thermodynamic suggests that the TZ dye adsorption on BC, MgO NPs, and BC@MgO NPs was spontaneous and endothermic. The TZ-loaded BC@MgO NPs was recycled and regenerated in six cycles with better adsorption efficiency. Under conditions optimal (C_0=50 mg L^{-1}, BC@MgO NPs dose=0.4 g L^{-1}, and pH=4), the TZ removal was 99.51 % with Box–Behnken design (BBD)-based optimization. The synthesis of BC@MgO NPs showed great potential adsorbent for dye removal from wastewaters

Keywords: Tartrazine dye; Biochar nanocomposite; Hydrothermal; Wastewater treatment; optimization

1 Introduction

Several health-related concerns have arisen because of the contaminants in the environment. Dyes are the major category of water resource contamination (Bashir et al., 2020; Dbik et al., 2022). The dyes cause cancer, mutagens, teratogens, cardiovascular shock, vomiting, gastrointestinal pain, diarrhea for human health (Bentahar et al., 2016), and water contamination with dyes causes severe environmental and aquatic life problems (El Messaoudi et al., 2021c). Among these dyes, tartrazine is an acidic azo dye (Arabzadeh et al., 2016) used in the food, cosmetics, pharmaceuticals, drugs, and textile industries (Khataei et al., 2020). Tartrazine can cause thyroid cancer, asthma, eczema, and migraines (Mittal et al., 2006). Great attention has been rewarded for developing new methods to remove toxic dyes from polluted water to overcome this severe problem. In this context, several techniques have been developed to remove dyes from an aqueous solution such as photocatalysis, degradation, coagulation, flocculation, hydrogen peroxide, ion exchange, reverse osmosis, membrane filtration, precipitation (Akpomie and Conradie, 2020; El Messaoudi et al., 2021e). Among them, adsorption is considered one of the most effective and widely used methods for the removal of dyes from industrial effluents (Dbik et al., 2014).

Eriobotrya *japonica* (also known as Loquat locally) belongs to *Rosaceae* family (Nazir et al., 2021). It is reported that loquat tree has high medicinal potential and possesses various biological activities such as antioxidant, antimicrobial, antitumor, antimutagenic, antiviral, and anti-inflammatory actions (Zheng et al., 2021). Biochar is a carbon-based material with a highly porous and functional surface. Since biochar can be obtained through the pyrolysis of biomass derived from plant and animal waste, such as timber, fruits, leaves, and bone. It provides an environment-friendly method for decontamination (Zheng et al., 2021). However, modification of biochar derived from *Eriobotrya japonica* leave with MgO nanoparticles for environmental purposes such as TZ removal from wastewater has rarely been studied.

Nanoparticles show very unique and enhanced physicochemical properties due to their sizes at the nanoscale (Bouich et al., 2019; Nazir et al., 2021). MgO, CuO, TiO_2, SiO_2, etc., have been used as nanoparticle absorbents (Liang and Esmaeili, 2021). Still, the efficacy of MgO is proved to be better due to its unique conductive nature and low cost (Xiang et al., 2017). Nanostructures of MgO and MgO nanocomposites have been developed by such reactions as solid-state, sonochemical, and ultrasonic-assisted approaches (Karthik et al., 2019; Zhang et al., 2019). Besides, the hydrothermal and sol-gel methods are regarded as simple, rapid, cost-effective, and eco-friendly methods for creating nanostructured materials such as metals, metal chalcogenides, and bimetal oxide (Cai et al., 2017).

In the present research, a novel nanocomposite is synthesized which could efficiently remove tetracycline (TC) from the solution aqueous. The current work will substantially impact as it will add unique knowledge on the adsorption potential of biochar prepared from *Eriobotrya japonica* leaves modified with MgO nanoparticles. In addition, characterization techniques were practiced for investigating its structure and properties, such as Fourier transform infrared spectroscopy coupled with total reflectance technique (FTIR-ATR), Brunauer-Emmett-Teller (BET), scanning electron microscope coupled with energy-dispersive X-ray (SEM-EDX), transition electron microscope (TEM), X-ray diffraction (XRD), and point of zero charge (PZC).

This study was conducted with the following objectives: (i) synthesis of novel nanocomposite BC@MgO NPs using hydrothermal method based on biochar derived from *Eriobotrya japonica* leaves and magnesium oxide nanoparticles (MgO NPs), (ii) characterization of BC@MgO NPs synthesized by various analytical techniques, (iii) investigation of the impact of various influencing experimental parameters (adsorbent dose, contact time, pH, TZ concentration and temperature), (iv) evaluation of this adsorption by kinetic and equilibrium models and thermodynamics parameters, (v) regeneration of BC@MgO NPs for its reusability for the TZ

removal, (vi) proposition of mechanism adsorption of TZ molecules on the BC@MgO NPs surface, and (vii) optimization of the adsorption process using Box–Behnken design (BBD).

2 Experimental

2.1 Chemicals

The magnesium chloride hexahydrate ($MgCl_2$, 6 H_2O), C_2H_5OH, distilled water, deionized water, HCl, KNO_3, NaOH, and tartrazine (anionic dye, $C_{16}H_9N_4Na_3O_9S_2$, CI=19140, MW=534.3 g mol^{-1}) are used chemicals used in this study.

2.2 Synthesis of adsorbent

2.2.1 Preparation of biochar from *Eriobotrya japonica* leaves

The naturally dried *Eriobotrya japonica* leaves (EJL) were obtained locally from Tinghir, Morocco. The biomaterial was crushed, sieved, and washed with C_2H_5OH, then dried at 105 °C for 12 h. *Eriobotrya japonica* leaves were pyrolyzed in the N_2 atmosphere and the heating temperature and residence time were set at 320 °C and 2h with a rate was 4 $^oC\ min^{-1}$. After that, the prepared biochar was cooled for 5 h.

2.2.2 Synthesis of MgO NPs

10 g of magnesium chloride hexahydrate ($MgCl_2$, 6 H_2O) was dissolved in 100 mL of deionized water, mixed with 50 mL of NaOH, and volume was made up 500 mL and stirred for 4 h. After precipitation, the gel was thus obtained and rinsed with deionized water. The MgO NPs dried at 60 °C for 24 h and were calcined in the furnace at 500 °C for 3 h.

2.2.3 Synthesis of BC@MgO NPs nanocomposite

2 g of biochar (BC) powder prepared and 1 g of MgO NPs were added into 50 mL of deionized water and stirred for 3 h (2:1 v/v). After that, placed in a solution of Teflon-sealed autoclave (50 mL) and was kept at 100 °C for 3 h. Then it was centrifuged and dried in an oven for 16 h at 80 °C. After all, the annealing process was conducted in a tube muffle furnace at 700 °C for 3 h to obtain the biochar nanocomposite (BC@MgO NPs).

2.3 Characterization

FTIR-ATR analysis (Jasco 4100) was used to determine the bond characteristics of BC, MgO NPs, BC@MgO NPs, and TZ-BC@MgO NPs. The BET (Belsorp Mini II) methods were employed to evaluate the surface area of the prepared materials. The XRD was recorded on a 6100-Shimadzu to evaluate the MgO NPs and BC@MgO NPs crystal structures. The morphologies of material adsorbents were observed using SEM-EDX analysis (JEOL, JSM-IT200) and TEM (Philips CM-30).

2.4 PZC of BC@MgO NPs

About 0.025 g of BC@MgO NPs were scattered into 50 mL of KNO_3 (0.03 M), and the pH was adjusted between 2 and 12 and denoted pH_i. Moreover, the suspensions were agitated by using a shaker at 25 ±1 °C for 24 h and denoted pH_f. The pH_i–pH_f was plotted against the first pH_i (Fiol and Villaescusa, 2009). The PZC was obtained at the intersection of the resulting curve.

2.5 Batch experimental studies

The adsorption behavior of BC, MgO NPs, and BC@MgO NPs towards TZ dye was experimentally investigated in a batch reactor under various operating conditions such as adsorbent dosage (0.1–0.7 g L^{-1}), solution pH (3–10), reaction time (5–120 min), and temperature (20–40 °C) were evaluated. After adsorption, the adsorbent was separated from the liquid phase using centrifuging. The concentration of TZ dye before and after adsorption was measured by a UV/Vis 2300 spectrophotometer at 426 nm. The adsorbed removal (%) and the quantity adsorbed q_e (mg g^{-1}) of TZ dye were calculated by Eqs. (1) and (2):

$$\% \, Removal = \frac{(C_0 - C_e)}{C_0} \times 100 \quad (1)$$

$$q_e = \frac{(C_0 - C_e) \times V}{m} \quad (2)$$

where C_0 (mg L^{-1}) is the initial TZ dye concentration and C_e (mg L^{-1}) is the TZ dye concentration at equilibrium. The m (g) is the masse of the adsorbent and V (L) is the volume of dye solution.

2.6 Process variables and experimental design

The experimental adsorption design was established using BBD implemented in design-expert software (version 12.0.3). The factors such as TZ dye concentration (X_1), pH (X_2), and BC@MgO NPs dose (X_3) have a significant effect on the TZ adsorption on BC@MgO NPs at 25±1°C for 50 min. The codes and variables of the BBD matrix and experimental data for TZ adsorption efficiency using BC@MgO NPs are presented in **Table 1**. Experiments were established based on a BBD with three factors (BC@MgO NPs dose (0.3-0.5 g L^{-1}), TZ concentration (50-150 mg L^{-1}), and pH (3-5)) and levels (–1, 0, and 1) consisting of 18 runs were designed to optimize TZ dye adsorption. The experimental results were statistically analyzed by second-order quadratic polynomial Eq. (3) (Jawad et al., 2020):

$$R(\%) = \beta_0 + \sum_{I=1}^{3} \beta_i X_i + \sum_{I=1}^{3} \beta_{ii} X_i^{\,2} + \sum_{I<j} \beta_{ij} X_i X_j \qquad (3)$$

where R (%) is the removal of the TZ as a response, X_i is the selected independent variables, β_0 constant-coefficient, β_i is the direct effect, β_{ii} is the higher-order effect, and β_{ij} is the reciprocate effect.

3 Results and discussion

3.1 Material characterization

The FTIR spectra of BC, MgO NPs, BC@MgO NPs, and TZ-BC@MgO NPs are presented in **Fig.1**. On the spectrum of BC, the peak at $\nu \sim 3330$ cm^{-1} confirmed the existence of the –OH group from the surface-absorbed water molecule group (Bentahar et al., 2019; Salomón et al., 2020). The asymmetric (2920 cm^{-1}) and symmetric (2860 cm^{-1}) of the –C–H deforming vibration are detected with weak intensity (Guo et al., 2016). The broad peaks (1700–

1000 cm^{-1}) for softwood biochars, attributed to the carbonyl/carboxyl C=O and aromatic C = C bonds (El Khomri et al., 2020). On the spectrum of MgO NPs, The peak found at 652 cm^{-1} can be ascribed to bending vibration of the Mg–O group (Priyadarshini et al., 2021) affirms the presence of the MgO group in the synthesized nanoparticles. The peak at 1393 cm^{-1} corresponds to the absorption of gas-phase CO_2 (Ahmed et al., 2021). On spectrum BC@MgO NPs, the new peaks that appeared on the surface at 653 cm^{-1} and 1395 cm^{-1} indicate the complexation of nanoparticles with BC. After TZ adsorption (TZ-BC@MgO NPs), a new band appears at ~1490 cm^{-1} (C=C stretch in the aromatic ring) can be assigned to the poly aromatic ring of TZ dye loaded on BC@MgO NPs surface.

The isotherms of adsorption and desorption of adsorbents are presented in **Fig.2**. Using the BET analysis, the surface area of BC, MgO NPs, and BC@MgO NPs were 69.45, 97.63, and 112.67 $m^2\ g^{-1}$, respectively. These values indicate the capillary condensation in the mesoporous of BC@MgO NPs than MgO and BC.

To determine the quality of microstructures, BC, MgO NPs, and BC@MgO NPS were examined by SEM analysis (**Fig.3**). From **Fig.3a**, the particles of BC are crystal of the structure. The SEM micrographs of MgO NPs showed that the particles exist in the form of a quasi-polyhedral shape with an average size between 0.5 and 5μm (**Fig. 3b**). **Fig.3c** shows the change of BC surface microspores due to the dispersion of MgO nanoparticles. This development indicates the successful deposition of the MgO NPs on the BC surface **Fig.3d** shows morphologic features of nanoparticles after adsorption of TZ.

EDX elemental analysis of BC@MgO NPs confirmed the complexation of MgO NPs with the surface of BC. According to **Fig.4**, BC@MgO NPs nanocomposite is composed of C (25.79%), O (61.20%), and Mg (13.01%). TEM images of MgO NPs and BC@MgO NPs nanocomposite are shown in **Fig.5** as observed MgO nanoparticles are crystal morphology and are immobilized on BC surface.

Fig.6 shows the XRD patterns of MgO NPs and BC@MgO NPs. On the pattern of MgO NPs, the strong and sharp peaks at 2θ=34.82, 41.13, 61.67, 74.82, and 78.69° are coincident with (111), (200), (220), (311), and (222) planes (JCPDS, No.76-0615), respectively, indicating successful synthesis of MgO crystals. Dummer et al. (Dummer et al., 2016) reported similar results. On the pattern of BC@MgO NPs the presence of Mg phase in BC@MgO NPs structure (JCPDS, No.01-84-1745), indicating the successful coating of MgO NPs to biochar surface.

3.2 Influence of operational parameters on TZ adsorption

3.2.1 Effect of adsorbent dose

The influence of adsorbent dosage (0.1–0.7 g L^{-1}) was examined in parameters keep constant (C_0=100 mg L^{-1}, t=120 min, T=25±1 °C, and pH (TZ)=4.78). **Fig.7** shows the results obtained. The TZ removal increased from 50.78 to 90.33 % for BC, from 64.60 to 93.23 % for MgO NPs, and from 71.52 to 98.41 % for BC@MgO NPs by increasing the adsorbent dose from 0.1 to 0.6 g L^{-1}, from 0.1 to 0.5 g L^{-1}, and from 0.1 to 0.4 g L^{-1}, respectively. Results imply that the number of active adsorption sites for TZ adsorption corresponds to the applied dose, which prompts higher removal efficiency (Hoang et al., 2020). After equilibrium between the adsorbent and dye in the solution, the removal percentage remains consistent at higher dosages, which is due to fixed TZ ions concentration in the liquid phase, as compared to higher adsorbent dose (El Messaoudi et al., 2017a). The optimum adsorbent dosage was considered 0.6 g L^{-1} for BC, 0.5 g L^{-1} for MgO NPs, and 0.4 g L^{-1} for BC@MgO NPs to reach maximum TZ removal efficiency.

3.2.2 Effect of reaction

The influence of the reaction time (5-120 min) on TZ adsorption using BC, MgO NPs, and BC@MgO NPs, whereas other parameters were kept constant (BC dose =0.6 g L^{-1}, MgO NPs dose =0.5 g L^{-1}, BC@MgO NPs dose=0.4 g L^{-1}, pH=4.78, and T =25±1°C). The results are displayed in **Fig.8**. The TZ adsorption was fast within the first 10 min for three adsorbents,

which could be due to many sites accessible on the surface of the adsorbent in the initial phase (El Messaoudi et al., 2021b). After that, the adsorption rate became consistent as a result of the progressive occupation of active sites of adsorbent over the contact time course (Aljeboree et al., 2017). Experimental data showed that equilibrium was achieved in 50 min with equilibrium adsorption capacities of TZ were 150.73, 180.88, and 226.10 mg g^{-1} for BC, MgO NPs, and BC@MgO NPs, respectively.

3.2.3 Effect of solution pH

The influence of solution pH on the TZ adsorption using BC, MgO NPs, and BC@MgO NPs was carried at different pH ranging from 3 to 10 (**Fig.9a**) at experimental conditions: C_0=100 mg L^{-1}, BC dose =0.6 g L^{-1}, MgO NPs dose =0.5 g L^{-1}, BC@MgO NPs dose=0.4 g L^{-1}, t=50 min, and T=25±1°C. The quantity adsorbed of TZ decreased drastically from 165.20 to 72.23 mg g^{-1} for BC, from 198.24 to 86.68 mg g^{-1} for MgO NPs, and from 247.81 to 108.35 mg g^{-1} for BC@MgO NPs upon increasing the pH from 3 to 10. A similar decreasing trend of TZ ions removal from wastewater has already been reported in the literature (Ebrahimpoor et al., 2021; Ouassif et al., 2020). The highest uptake quantity of TZ in the acidic medium can be explained by the existence of electrostatic attraction forces between charge positive of adsorbent and the charge negative of TZ (TZH^-, TZ^-), while the opposite is in the basic medium (Sahnoun and Boutahala, 2018). The highest q_e of was 241.48 mg g^{-1} at pH=4. As **Fig.9b** shows, PZC of BC@MgO NPs was 8.7. The dominance of charge positive of BC@MgO NPs at pH<PZC (adsorption of TZ was favorable) and negatively charged when pH>PZC (adsorption of TZ was unfavorable) (Huang et al., 2019).

3.2.4 Effect of TZ concentration

Fig.10 shows the impact of TZ concentration in the range of 50–400 mg L^{-1} on TZ adsorption with a fixed pH of 4 and adsorbent dose of 0.6 g L^{-1} for BC, 0.5 g L^{-1} for MgO NPs, and 0.4 g L^{-1} for BC@MgO NPs for 50 min. As illustrated in **Fig.10**, by increasing TZ concentration from 50 to 200 mg L^{-1} for BC, from 50 to 250 mg L^{-1} for MgO NPs, and from 50 to 300 mg L^{-}

^{1} for BC@MgO NPs, the TZ adsorption capacity progressively increased from 80.73 to 281.86 mg g^{-1}, from 97.16 to 436.04 mg g^{-1}, and from 117.66 to 624.40 mg g^{-1}, respectively. This increases due to the occupation of all available sites on the adsorbent surface by TZ molecules (Dbik et al., 2020). After initial TZ concentration of 200 mg L^{-1} for BC, 250 mg L^{-1} for MgO NPs, and 300 mg L^{-1} for BC@MgO NPs, the adsorption capacity almost was achieved in the adsorption capacity due to still available of active sites at the surface adsorbents (El Khomri et al., 2021b; Jarrah and Farhadi, 2020).

3.2.5 Effect of temperature

Temperature is also one of the most critical parameters that could significantly affect the adsorption behavior of pollutants (El Messaoudi et al., 2022). In this context, the effect of temperature on the adsorption capacities of TZ on BC and MgO NPs, and BC@MgO NPs was studied in the range 20-40 °C at C_0=100 mg L^{-1}, BC dose=0.6 g L^{-1}, MgO NPs dose=0.5 g L^{-1}, BC@MgO NPs dose=0.4 g L^{-1}, t=50 min and pH=4. As demonstrated in **Fig.11**, the quantity adsorbed of TZ increased from 125.56 to 180.46 mg g^{-1} for BC, from 176.47 to 212.21 mg g^{-1} for MgO NPs, and from 231.02 to 267.16 mg g^{-1} for BC@MgO NPs with increasing the temperature from 20 to 40 °C. This increases the quantity of adsorbed due to the increased mobility of TZ molecules and active sites at the surface of adsorbents at higher temperatures (El Messaoudi et al., 2021a).

3.3 Adsorption modeling

3.3.1 Kinetic modeling

The adsorption kinetic models were applied to interpret the experimental data to determine the controlling mechanism of dye adsorption from an aqueous solution (Khomri et al., 2022). The pseudo 1st order (PFO), pseudo 2nd order (PSO), and Elovich kinetic models were used to evaluate adsorption kinetic of TZ on BC, MgO NPs, and BC@MgO NPs and given using the

following Eqs. (4), (5), and (6), respectively (Ho and McKay, 1998; Simonin, 2016; Wu et al., 2009):

$$Log(q_e - q_t) = Log(q_e) - \frac{K_{PFO}}{2.303}t \quad (4)$$

$$\frac{t}{q_t} = \frac{1}{K_{PSO}{q_e}^2} + \frac{1}{q_e}t \quad (5)$$

$$q_t = \frac{1}{\beta_e}ln(\alpha_e\beta_e) + \frac{1}{\beta_e}\ lnt \quad (6)$$

In Eqs. (4), (5), and (6), K_{PFO} (min^{-1}) and K_{PSO} (g mg^{-1} min^{-1}) denote the PFO and PSO rate constants of kinetic models, respectively, α_e (mg g^{-1} min^{-1}) and β_e (g mg^{-1}) denote the Elovich coefficients. **Table 2** shows the parameters for linear fitting. By comparing the values of correlation coefficient R^2, the PSO model is more suitable than the PFO and Elovich models for three adsorbents. In addition, the experimental $q_{e,exp}$ values are also closer to the theoretically calculated $q_{e,cal}$ values for the PSO. Therefore, the adsorption of tartrazine on BC, MgO NPs, and BC@MgO NPs was better described by the kinetic PSO model.

3.3.2 Isotherm modeling

The adsorption isotherm modeling help to understand the distribution between the adsorbent and adsorbate. The TZ adsorption on BC, MgO NPs, and BC@MgO NPs was evaluated by three isotherm models such as Langmuir, Freundlich, and Temkin, and given using the following Eqs. (7), (8), and (9), respectively (Freundlich, 1907; Johnson and Arnold, 1995; Langmuir, 1918):

$$\frac{C_e}{q_e} = \frac{1}{Q_m K_L} + \frac{C_e}{Q_m} \quad (7)$$

$$Lnq_e = LnK_F + \frac{LnC_e}{n} \quad (8)$$

$$q_e = BLnK_T + BLnC_e \quad (9)$$

In Eqs. (7), (8), and (9), Q_m (mg g^{-1}) and C_e (mg L^{-1}) denote the monolayer (maximum) adsorption capacity and equilibrium concentration of TZ, K_L (L mg^{-1}), K_F (mg g^{-1}) and K_T (L

g^{-1}) denote the Langmuir, Freundlich, and Temkin rate constants, respectively, n is the heterogeneity factor and *B* is the constant related to heat adsorption. **Table 3** shows the parameters for linear fitting. Based on correlation coefficients R^2, the Langmuir model best described the TZ adsorption equilibrium. The *Qm* of BC, MgO NPs, and BC@MgO NPs for TZ removal were 313.74, 480.76, and 643.50 mg g^{-1}, respectively at 25 °C. Therefore this model suggests a monolayer adsorption process (Jerold et al., 2017). A similar observation was found in other studies (Duan et al., 2019; Sahnoun and Boutahala, 2018). The comparison of the maximum adsorption of BC, MgO NPS, and BC@MgO NPS to remove TC from aqueous solution with other adsorbents reported in the literature is represented in **Table 4**. This research illustrated the capability of BC@MgO NPs to remove tartrazine from wastewater.

3.4 Thermodynamic parameters

The parameters such $\Delta G°$ (kJ mol^{-1}), $\Delta H°$ (kJ mol^{-1}), and $\Delta S°$ (J mol^{-1} K^{-1}) of TZ adsorption on adsorbents were calculated by Eq. (10) and (11) (El Khomri et al., 2021a) :

$$\Delta G° = -RTLnK_C \tag{10}$$

$$LnK_C = \frac{\Delta S°}{R_{gas}} - \frac{\Delta H°}{RT} \tag{11}$$

In Eq. (10) and (11), *T* (K) denotes the temperature, R_{gas} represents the universal gas constant (8.314 J mol^{-1} K^{-1}), and K_C is the equilibrium coefficient. The thermodynamic adsorption parameters of TZ on adsorbents are given in **Table 5**. The values of $\Delta H°$ are positive, implying that adsorption of TZ onto BC, MgO NPS, and BC@Mgo NPS is an endothermic process (Song et al., 2015). This highlighted that the adsorption process prefers higher temperatures. The positive values of $\Delta S°$ suggest that the TZ dye adsorption is accompanied by increasing randomness at the adsorbent-solution interphase (El Messaoudi et al., 2017b). The negative value of ΔG° at three temperatures (293, 303, and 313 K) for the BC, MgO, and BC@MgO NPs, suggested the feasibility and spontaneity of the TZ adsorption on adsorbents (Saber-

Samandari et al., 2014). The physisorption can be the dominant mechanism because the $\Delta G°$ values were lower than 0 kJ mol^{-1} (Hao et al., 2020).

3.5 Proposed adsorption mechanism

Several mechanisms have been reported to explain the adsorption of TZ dye (Ali et al., 2022; Arabzadeh et al., 2014; Hu et al., 2017). The proposed interactions between the TZ molecules dye and the BC@MgO NPs are schematized in **Fig.12**. The adsorption efficiency of TZ on BC@MgO NPs occurred at pH<PZC (8.7) due to the positively charged nanocomposite, thus electrostatic interactions are governed between TZ molecules and the surface of the adsorbent.

3.6 Regeneration and reusability

The reusability of a nanocomposite is a crucial criterion for the application at an industrial scale. For this purpose, the regeneration of BC@MgO NPs for the removal of TZ was investigated using 0.1 M NaOH and the experimental data are presented in **Fig.13**. The adsorption rate of TZ still was maintained at 90.11 % after six successive adsorption-desorption cycles with decreases of 9.17 % report to the first cycle at optimal conditions (BC@MgO NPs dose of 0.4 g L^{-1}, time of 50 min, TZ concentration of 100 mg L^{-1}, pH of 4, and temperature of 25±1°C). This decrease was attributed to the occupation of available sites on the BC@MgO NPs surface (El Messaoudi et al., 2021d). These results indicated that the BC@MgO NPs is a durable material for regeneration studies.

3.7 Box-Behnken design-based optimization

To study the combined effect of independent variables on the removal of TZ using BC@MgO NPs, experiments were performed for different combinations of the physical parameters using statistically designed experiments and the results are shown in **Table 6**. The quadratic response model is represented below in Eq. (12):

$$R\,(\%) = 98.42 - 7.42\,X_1 + 1.96\,X_2 - 0.7017\,X_3 + 2.82\,X_1X_2 - 1.21X_1X_3 - 1.67\,X_2X_3 - 3.20\,X_1^2 - 5.81\,X_2^2 + 0.1154\,X_3^2 \quad (12)$$

The corresponding p-value (less than 0.0001) (Qu et al., 2017). These values indicate that the model is significant. The high correlation coefficient (R^2=0.9810) indicates the excellent optimization of TZ adsorption based on BBD-RSM. The value of adequate precision of 18.0480 (>4) shows a high level of statistical significance (Wan et al., 2018). Actual *vs.* predicted and 3D response surface curves are illustrated in **Fig.14**. From **Fig.14 a,** it can be seen that the actual values of the TZ removal efficiency were close to the straight line. This is indicative that the experimental data are in line with the designed model (Dbik et al., 2022). From **Fig.14 b, c,** and **d,** the three factors **(**BC@MgO NPs dose, pH, and TZ concentration) chosen had a reasonable impact on the response. The 3D response surface plot reveals that the CV adsorption performance increases with increasing BC@MgO NPs dosage and TZ dye concentration while decreasing with increasing pH of the solution (Nguyen et al., 2021). Under optimal conditions, the TZ removal was 99.51 % set as BC@MgO NPs dose of 0.4 g L^{-1}, TZ concentration of 50 mg L^{-1}, and pH of 4 at 25±1°C for 50 min with BBD-RSM modeling.

4 Conclusions

The novel nanocomposite was fabricated from the biochar modified by MgO nanoparticles and employed for TZ removal. The result of FTIR, SEM-EDX, TEM, and XRD characterization verified the dispersion and complexation of MgO nanoparticles with BC. Under conditions, the TZ removal was more than 90 % for BC, 93 % for MgO NPS, and 98 % for BC@MgO NPS. The experimental kinetic data were described well in the PSO model and followed and Langmuir model. The *Qm* was 313.74 mg g^{-1} for BC, 480.76 mg g^{-1} for MgO NPs, and 643.50 mg g^{-1} for BC@Mgo NPS at 25 °C. The TZ adsorption on BC, MgO NPS, and BC@Mgo NPS nanocomposite was spontaneous, endothermic, and physical. The results shed light on the adsorption mechanism, while the electrostatic interactions are the foremost driving force when TZ dye adsorbs onto BC@MgO NPs nanocomposite. The regeneration study demonstrated that the BC@MgO NPs nanocomposite exhibits good reusability potential. Optimization is a

practical approach for modeling the sorption process of the TZ on BC@MgO NPs using BBD–RSM. From these results, the BC@MgO NPs nanocomposite can be competitive candidates for the efficient treatment of hazardous synthetic dyes from wastewater.

References

Ahmed, T., Noman, M., Shahid, M., Shahid, M.S., Li, B., 2021. Antibacterial potential of green magnesium oxide nanoparticles against rice pathogen Acidovorax oryzae. Mater. Lett. 282, 128839. https://doi.org/10.1016/j.matlet.2020.128839

Akpomie, K.G., Conradie, J., 2020. Banana peel as a biosorbent for the decontamination of water pollutants. A review. Environ. Chem. Lett. https://doi.org/10.1007/s10311-020-00995-x

Ali, M.A., Mubarak, M.F., Keshawy, M., Zayed, M.A., Ataalla, M., 2022. Adsorption of Tartrazine anionic dye by novel fixed bed Core-Shell- polystyrene Divinylbenzene/Magnetite nanocomposite. Alexandria Eng. J. 61, 1335–1352. https://doi.org/10.1016/J.AEJ.2021.06.016

Aljeboree, A.M., Alshirifi, A.N., Alkaim, A.F., 2017. Kinetics and equilibrium study for the adsorption of textile dyes on coconut shell activated carbon. Arab. J. Chem. 10, S3381–S3393. https://doi.org/10.1016/j.arabjc.2014.01.020

Arabzadeh, N., Khosravi, A., Mohammadi, A., Mahmoodi, N.M., 2016. Enhanced photodegradation of hazardous tartrazine by composite of nanomolecularly imprinted polymer-nanophotocatalyst with high efficiency. Desalin. Water Treat. 57, 3142–3151. https://doi.org/10.1080/19443994.2014.989414

Arabzadeh, N., Khosravi, A., Mohammadi, A., Mahmoodi, N.M., 2014. Enhanced photodegradation of hazardous tartrazine by composite of nanomolecularly imprinted polymer-nanophotocatalyst with high efficiency. New pub Balaban 57, 3142–3151. https://doi.org/10.1080/19443994.2014.989414

Bagtash, M., Zolgharnein, J., 2018. Crossed mixture-process design for optimization of simultaneous adsorption of Tartrazine and Indigo carmine dyes by cobalt hydroxide nanosorbent. J. Chemom. 32, e3039. https://doi.org/10.1002/cem.3039

Bashir, I., Lone, F.A., Bhat, R.A., Mir, S.A., Dar, Z.A., Dar, S.A., 2020. Concerns and Threats of Contamination on Aquatic Ecosystems 1–26. https://doi.org/10.1007/978-3-030-35691-0_1

Bentahar, S., Dbik, A., El Khomri, M., El Messaoudi, N., Bakiz, B., Lacherai, A., 2016. Study of removal of Congo red by local natural clay. Sci. Study Res. Chem. Chem. Eng. Biotechnol. Food Ind. 17.

Bentahar, S., Taleb, M.A., Sabour, A., Dbik, A., El Khomri, M., El Messaoudi, N., Lacherai, A., Mamouni, R., 2019. Potassium Fluoride-Modified Clay as a Reusable Heterogeneous Catalyst for One-Pot Synthesis of 3,4-Dihydropyrimidin-2(1H)-ones. Russ. J. Org. Chem. 55. https://doi.org/10.1134/S1070428019090240

Bouich, A., Hartiti, B., Ullah, S., Ullah, H., Ebn Touhami, M., Santos, D.M.F., Mari, B., 2019. Optoelectronic characterization of CuInGa(S)2 thin films grown by spray pyrolysis for photovoltaic application. Appl. Phys. A 2019 1258 125, 1–9. https://doi.org/10.1007/S00339-019-2874-4

Cai, Y., Wu, D., Zhu, X., Wang, W., Tan, F., Chen, J., Qiao, X., Qiu, X., 2017. Sol-gel preparation of Ag-doped MgO nanoparticles with high efficiency for bacterial inactivation. Ceram. Int. 43, 1066–1072. https://doi.org/10.1016/j.ceramint.2016.10.041

Dbik, A., Bentahar, S., El Messaoudi, N., El Khomri, Mohammed;, Lacherai, A., 2020.

Removal of Methylene Blue from Aqueous Solution by Tunics of the Corm of the Saffron. Iran. J. Chem. Chem. Eng. 39, 95–104. https://doi.org/10.30492/IJCCE.2020.106169.3544

Dbik, A., El Messaoudi, N., Lacherai, A., 2014. Valorisation of wood dates stones of a variety of palm tree of Tinghir region (Morocco): Application to eliminate methylene blue. J. Mater. Environ. Sci. 5, 2510–2514.

Dbik, A., Messaoudi, N. El, Bentahar, S., Khomri, M. El, Lacherai, A., Faska, N., 2022. Optimization of Methylene Blue Adsorption on Agricultural Solid Waste Using Box-Behnken Design (BBD) Combined with Response Surface Methodology (RSM) Modeling 12, 4567–4583. https://doi.org/10.33263/BRIAC124.45674583

Duan, Y., Song, Y., Zhou, L., 2019. Facile synthesis of polyamidoamine dendrimer gel with multiple amine groups as a super adsorbent for highly efficient and selective removal of anionic dyes. J. Colloid Interface Sci. 546, 351–360. https://doi.org/10.1016/j.jcis.2019.03.073

Dummer, N.F., Joyce, L., Ellicott, H., Jiang, Y., 2016. Surfactant controlled magnesium oxide synthesis for base catalysis. Catal. Sci. Technol. 6, 1903–1912. https://doi.org/10.1039/c5cy01107h

Ebrahimpoor, S., Kiarostami, V., Khosravi, M., Davallo, M., Ghaedi, A., 2021. Optimization of Tartrazine Adsorption onto Polypyrrole/SrFe12O19/Graphene Oxide Nanocomposite Using Central Composite Design and Bat Inspired Algorithm with the Aid of Artificial Neural Networks. Fibers Polym. 22, 159–170. https://doi.org/10.1007/s12221-021-8163-9

El Khomri, M., El Messaoudi, N., Dbik, A., Bentahar, S., Lacherai, A., 2020. Efficient adsorbent derived from Argania Spinosa for the adsorption of cationic dye: Kinetics, mechanism, isotherm and thermodynamic study. Surfaces and Interfaces 20, 100601. https://doi.org/10.1016/j.surfin.2020.100601

El Khomri, M., El Messaoudi, N., Dbik, A., Bentahar, S., Lacherai, A., Chegini, Z.G., Bouich, A., 2021a. Removal of Congo red from aqueous solution in single and binary mixture systems using Argan nutshell wood. Pigment Resin Technol. https://doi.org/10.1108/PRT-04-2021-0045/FULL/XML

El Khomri, M., El Messaoudi, N., Dbik, A., Bentahar, S., Lacherai, A., Faska, N., Jada, A., 2021b. Regeneration of argan nutshell and almond shell using HNO3 for their reusability to remove cationic dye from aqueous solution. https://doi.org/10.1080/00986445.2021.1963960.

El Messaoudi, N., Dbik, A., El Khomri, M., Sabour, A., Bentahar, S., Lacherai, A., 2017a. Date stones of Phoenix dactylifera and jujube shells of Ziziphus lotus as potential biosorbents for anionic dye removal. Int. J. Phytoremediation 19, 1047–1052. https://doi.org/10.1080/15226514.2017.1319331

El Messaoudi, N., El Khomri, M., Ablouh, E.H., Bouich, A., Lacherai, A., Jada, A., Lima, E.C., Sher, F., 2022. Biosynthesis of SiO2 nanoparticles using extract of Nerium oleander leaves for the removal of tetracycline antibiotic. Chemosphere 287, 132453. https://doi.org/10.1016/J.CHEMOSPHERE.2021.132453

El Messaoudi, N., El Khomri, M., Chegini, Z.G., Bouich, A., Dbik, A., Bentahar, S., Labjar, N., Iqbal, M., Jada, A., Lacherai, A., 2021a. Dye removal from aqueous solution using nanocomposite synthesized from oxalic acid-modified agricultural solid waste and ZnFe2O4 nanoparticles. Nanotechnol. Environ. Eng. 2021 71 7, 1–15. https://doi.org/10.1007/S41204-021-00173-6

El Messaoudi, N., El Khomri, M., Chegini, Z.G., Dbik, A., Bentahar, S., Iqbal, M., Jada, A., Lacherai, A., 2021b. Desorption of crystal violet from alkali-treated agricultural material waste: an experimental study, kinetic, equilibrium and thermodynamic modeling. Pigment & Resin Technol. ahead-of-print. https://doi.org/10.1108/PRT-02-2021-0019

El Messaoudi, N., El Khomri, M., Chlif, N., Chegini, Z.G., Dbik, A., Bentahar, S., Lacherai, A., 2021c. Desorption of Congo red from dye-loaded Phoenix dactylifera date stones and Ziziphus lotus jujube shells. Groundw. Sustain. Dev. 12, 100552. https://doi.org/10.1016/j.gsd.2021.100552

El Messaoudi, N., El Khomri, M., Dabagh, A., Chegini, Z.G., Dbik, A., Bentahar, S., Lacherai, A., Iqbal, M., Jada, A., Sher, F., Lima, É.C., 2021d. Synthesis of a novel nanocomposite based on date stones/$CuFe_2O_4$ nanoparticles for eliminating cationic and anionic dyes from aqueous solution. Int. J. Environ. Stud. 1–19. https://doi.org/10.1080/00207233.2021.1929469

El Messaoudi, N., El Khomri, M., Dbik, A., Bentahar, S., Lacherai, A., 2017b. Selective and competitive removal of dyes from binary and ternary systems in aqueous solutions by pretreated jujube shell (Zizyphus lotus). J. Dispers. Sci. Technol. 38, 1168–1174. https://doi.org/10.1080/01932691.2016.1228070

El Messaoudi, N., El Khomri, M., Goodarzvand Chegini, Z., Chlif, N., Dbik, A., Bentahar, S., Iqbal, M., Jada, A., Lacherai, A., 2021e. Desorption study and reusability of raw and H_2SO_4 modified jujube shells (*Zizyphus lotus*) for the methylene blue adsorption. Int. J. Environ. Anal. Chem. 1–17. https://doi.org/10.1080/03067319.2021.1912338

Fiol, N., Villaescusa, I., 2009. Determination of sorbent point zero charge: Usefulness in sorption studies. Environ. Chem. Lett. 7, 79–84. https://doi.org/10.1007/s10311-008-0139-0

Freundlich, H., 1907. Über die Adsorption in Lösungen. Zeitschrift für Phys. Chemie 57U, 385–470. https://doi.org/10.1515/ZPCH-1907-5723

Guo, H., Yan, L., Song, D., Li, K., 2016. Citric acid modified Camellia oleifera shell for removal of crystal violet and Pb(II): parameters study and kinetic and thermodynamic profile. Desalin. Water Treat. 57, 15373–15383. https://doi.org/10.1080/19443994.2015.1072057

Habila, M.A., Alothman, Z.A., Ali, R., Ghafar, A.A., Hassouna, M.S.E.D., 2014. Removal of Tartrazine Dye onto Mixed-Waste Activated Carbon: Kinetic and Thermodynamic Studies. Clean - Soil, Air, Water 42, 1824–1831. https://doi.org/10.1002/clen.201300191

Hao, X., Song, X., Li, Kai, Wang, C., Li, Kunlin, Li, Y., Sun, X., Ning, P., 2020. Theoretical study on NO: X adsorption properties over the α-MnO2(110) surface. RSC Adv. 10, 9539–9548. https://doi.org/10.1039/c9ra09455e

Ho, Y.S., McKay, G., 1998. Sorption of dye from aqueous solution by peat. Chem. Eng. J. 70, 115–124. https://doi.org/10.1016/S0923-0467(98)00076-1

Hoang, L.P., Van, H.T., Hang Nguyen, T.T., Nguyen, V.Q., Thang, P.Q., 2020. Coconut shell activated carbon/CoFe2O4 composite for the removal of rhodamine B from aqueous solution. J. Chem. 2020. https://doi.org/10.1155/2020/9187960

Hu, D., Wan, X., Li, X., Liu, J., Zhou, C., 2017. Synthesis of water-dispersible poly-l-lysine-functionalized magnetic Fe3O4-(GO-MWCNTs) nanocomposite hybrid with a large surface area for high-efficiency removal of tartrazine and Pb(II). Int. J. Biol. Macromol. 105, 1611–1621. https://doi.org/10.1016/J.IJBIOMAC.2017.03.010

Huang, B., Liu, Y., Li, B., Wang, H., Zeng, G., 2019. Adsorption mechanism of polyethyleneimine modified magnetic core-shell Fe3O4@SiO2 nanoparticles for anionic dye removal. RSC Adv. 9, 32462–32471. https://doi.org/10.1039/c9ra06299h

Jarrah, A., Farhadi, S., 2020. Preparation and characterization of novel polyoxometalate/CoFe2O4/metal-organic framework magnetic core-shell nanocomposites for the rapid removal of organic dyes from water. RSC Adv. 10, 39881–39893. https://doi.org/10.1039/d0ra04603e

Jawad, A.H., Malek, N.N.A., Abdulhameed, A.S., Razuan, R., 2020. Synthesis of Magnetic Chitosan-Fly Ash/Fe3O4 Composite for Adsorption of Reactive Orange 16 Dye: Optimization by Box–Behnken Design. J. Polym. Environ. 28, 1068–1082.

https://doi.org/10.1007/s10924-020-01669-z
Jerold, M., Vasantharaj, K., Joseph, D., Sivasubramanian, V., 2017. Fabrication of hybrid biosorbent nanoscale zero-valent iron-Sargassum swartzii biocomposite for the removal of crystal violet from aqueous solution. Int. J. Phytoremediation 19, 214–224. https://doi.org/10.1080/15226514.2016.1207607
Johnson, R.D., Arnold, F.H., 1995. The temkin isotherm describes heterogeneous protein adsorption. Biochim. Biophys. Acta - Protein Struct. Mol. Enzymol. 1247, 293–297. https://doi.org/10.1016/0167-4838(95)00006-G
Karthik, K., Dhanuskodi, S., Gobinath, C., Prabukumar, S., Sivaramakrishnan, S., 2019. Ultrasonic-assisted CdO–MgO nanocomposite for multifunctional applications. Mater. Technol. 34, 403–414. https://doi.org/10.1080/10667857.2019.1574963
Khataei, M.M., Yamini, Y., Asiabi, H., Shamsayei, M., 2020. Covalent organic framework and montomorillonite nanocomposite as advanced adsorbent: synthesis, characterization, and application in simultaneous adsorption of cationic and anionic dyes. J. Environ. Heal. Sci. Eng. 18, 1555–1567. https://doi.org/10.1007/s40201-020-00572-y
Khomri, M. El, Messaoudi, N. El, Dbik, A., Bentahar, S., Lacherai, A., Goodarzvand Chegini, Z., 2022. Organic Dyes Adsorption on the Almond Shell (Prunus dulcis) as Agricultural Solid Waste from Aqueous Solution in Single and Binary Mixture Systems 12, 2022–2040. https://doi.org/10.33263/BRIAC122.20222040
Langmuir, I., 1918. The adsorption of gases on plane surfaces of glass, mica and platinum. J. Am. Chem. Soc. 40, 1361–1403. https://doi.org/10.1021/JA02242A004
Liang, H., Esmaeili, H., 2021. Application of nanomaterials for demulsification of oily wastewater: A review study. Environ. Technol. Innov. https://doi.org/10.1016/j.eti.2021.101498
Mittal, A., Mittal, J., Kurup, L., 2006. Adsorption isotherms, kinetics and column operations for the removal of hazardous dye, Tartrazine from aqueous solutions using waste materials-Bottom Ash and De-Oiled Soya, as adsorbents. J. Hazard. Mater. 136, 567–578. https://doi.org/10.1016/j.jhazmat.2005.12.037
Nazir, A., Akbar, A., Baghdadi, H.B., ur Rehman, S., Al-Abbad, E., Fatima, M., Iqbal, M., Tamam, N., Alwadai, N., Abbas, M., 2021. Zinc oxide nanoparticles fabrication using Eriobotrya japonica leaves extract: Photocatalytic performance and antibacterial activity evaluation. Arab. J. Chem. 14, 103251. https://doi.org/10.1016/J.ARABJC.2021.103251
Nguyen, D.T.C., Dang, H.H., Vo, D.V.N., Bach, L.G., Nguyen, T.D., Tran, T. Van, 2021. Biogenic synthesis of MgO nanoparticles from different extracts (flower, bark, leaf) of Tecoma stans (L.) and their utilization in selected organic dyes treatment. J. Hazard. Mater. 404, 124146. https://doi.org/10.1016/J.JHAZMAT.2020.124146
Ouassif, H., Moujahid, E.M., Lahkale, R., Sadik, R., Bouragba, F.Z., Sabbar, E. mouloudi, Diouri, M., 2020. Zinc-Aluminum layered double hydroxide: High efficient removal by adsorption of tartrazine dye from aqueous solution. Surfaces and Interfaces 18, 100401. https://doi.org/10.1016/j.surfin.2019.100401
Priyadarshini, B., Patra, T., Sahoo, T.R., 2021. An efficient and comparative adsorption of Congo red and Trypan blue dyes on MgO nanoparticles: Kinetics, thermodynamics and isotherm studies. J. Magnes. Alloy. 9, 478–488. https://doi.org/10.1016/j.jma.2020.09.004
Qu, J., Meng, X., You, H., Ye, X., Du, Z., 2017. Utilization of rice husks functionalized with xanthates as cost-effective biosorbents for optimal Cd(II) removal from aqueous solution via response surface methodology. Bioresour. Technol. 241, 1036–1042. https://doi.org/10.1016/j.biortech.2017.06.055
Saber-Samandari, Samaneh, Saber-Samandari, Saeed, Nezafati, N., Yahya, K., 2014. Efficient removal of lead (II) ions and methylene blue from aqueous solution using chitosan/Fe-hydroxyapatite nanocomposite beads. J. Environ. Manage. 146, 481–490. https://doi.org/10.1016/j.jenvman.2014.08.010

Sahnoun, S., Boutahala, M., 2018. Adsorption removal of tartrazine by chitosan/polyaniline composite: Kinetics and equilibrium studies. Int. J. Biol. Macromol. 114, 1345–1353. https://doi.org/10.1016/j.ijbiomac.2018.02.146

Salomón, Y.L. d. O., Georgin, J., Franco, D.S.P., Netto, M.S., Grassi, P., Piccilli, D.G.A., Oliveira, M.L.S., Dotto, G.L., 2020. Powdered biosorbent from pecan pericarp (Carya illinoensis) as an efficient material to uptake methyl violet 2B from effluents in batch and column operations. Adv. Powder Technol. 31, 2843–2852. https://doi.org/10.1016/j.apt.2020.05.004

Simonin, J.P., 2016. On the comparison of pseudo-first order and pseudo-second order rate laws in the modeling of adsorption kinetics. Chem. Eng. J. 300, 254–263. https://doi.org/10.1016/J.CEJ.2016.04.079

Song, N., Wu, X.L., Zhong, S., Lin, H., Chen, J.R., 2015. Biocompatible G-Fe3O4/CA nanocomposites for the removal of Methylene Blue. J. Mol. Liq. 212, 63–69. https://doi.org/10.1016/j.molliq.2015.08.059

Wan, Y., Liu, X., Liu, P., Zhao, L., Zou, W., 2018. Optimization adsorption of norfloxacin onto polydopamine microspheres from aqueous solution: Kinetic, equilibrium and adsorption mechanism studies. Sci. Total Environ. 639, 428–437. https://doi.org/10.1016/j.scitotenv.2018.05.171

Wu, F.C., Tseng, R.L., Juang, R.S., 2009. Characteristics of Elovich equation used for the analysis of adsorption kinetics in dye-chitosan systems. Chem. Eng. J. 150, 366–373. https://doi.org/10.1016/J.CEJ.2009.01.014

Xiang, M., Wu, H., Liu, Heng, Huang, J., Zheng, Y., Yang, L., Jing, P., Zhang, Y., Dou, S., Liu, Huakun, 2017. A Flexible 3D Multifunctional MgO-Decorated Carbon Foam@CNTs Hybrid as Self-Supported Cathode for High-Performance Lithium-Sulfur Batteries. Adv. Funct. Mater. 27, 1702573. https://doi.org/10.1002/adfm.201702573

Zandipak, R., Sobhanardakani, S., 2016. Synthesis of NiFe2O4 nanoparticles for removal of anionic dyes from aqueous solution. Desalin. Water Treat. 57, 11348–11360. https://doi.org/10.1080/19443994.2015.1050701

Zhang, H., Hu, J., Xie, J., Wang, S., Cao, Y., 2019. A solid-state chemical method for synthesizing MgO nanoparticles with superior adsorption properties. RSC Adv. 9, 2011–2017. https://doi.org/10.1039/C8RA09199D

Zheng, Z., Ali, A., Su, J., Fan, Y., Zhang, S., 2021. Layered double hydroxide modified biochar combined with sodium alginate: A powerful biomaterial for enhancing bioreactor performance to remove nitrate. Bioresour. Technol. 323, 124630. https://doi.org/10.1016/J.BIORTECH.2020.124630

List of Figures

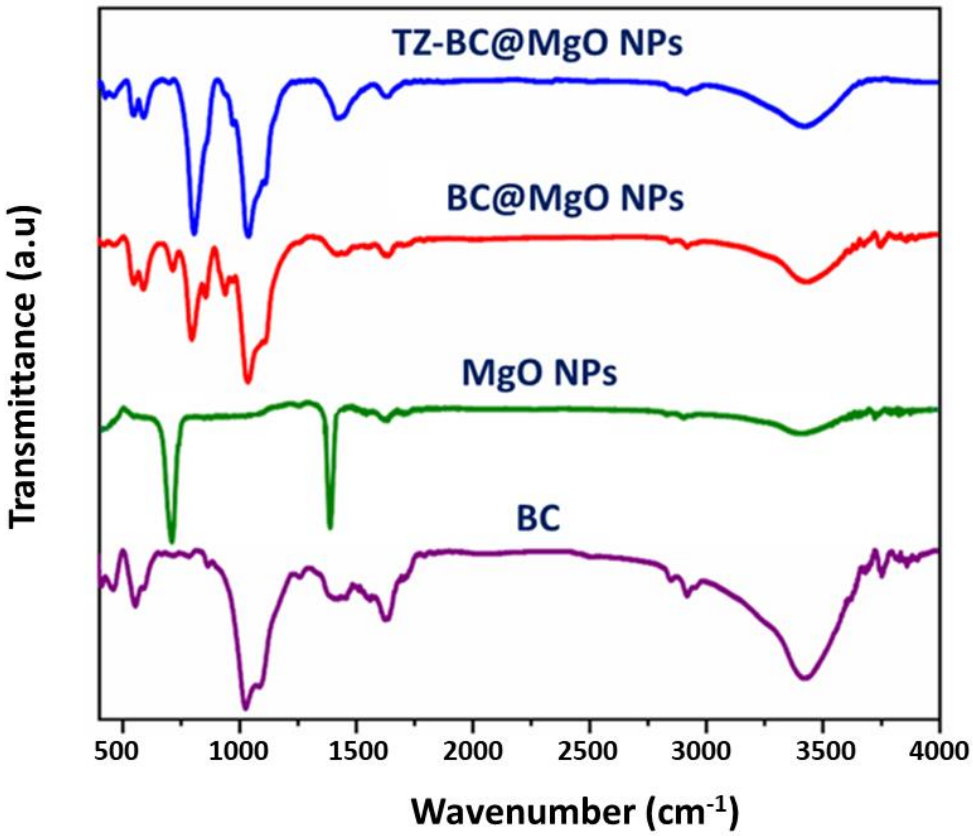

Fig.1. FTIR spectra of BC, MgO NPs, BC@MgO NPs, and TZ-BC@MgO NPs.

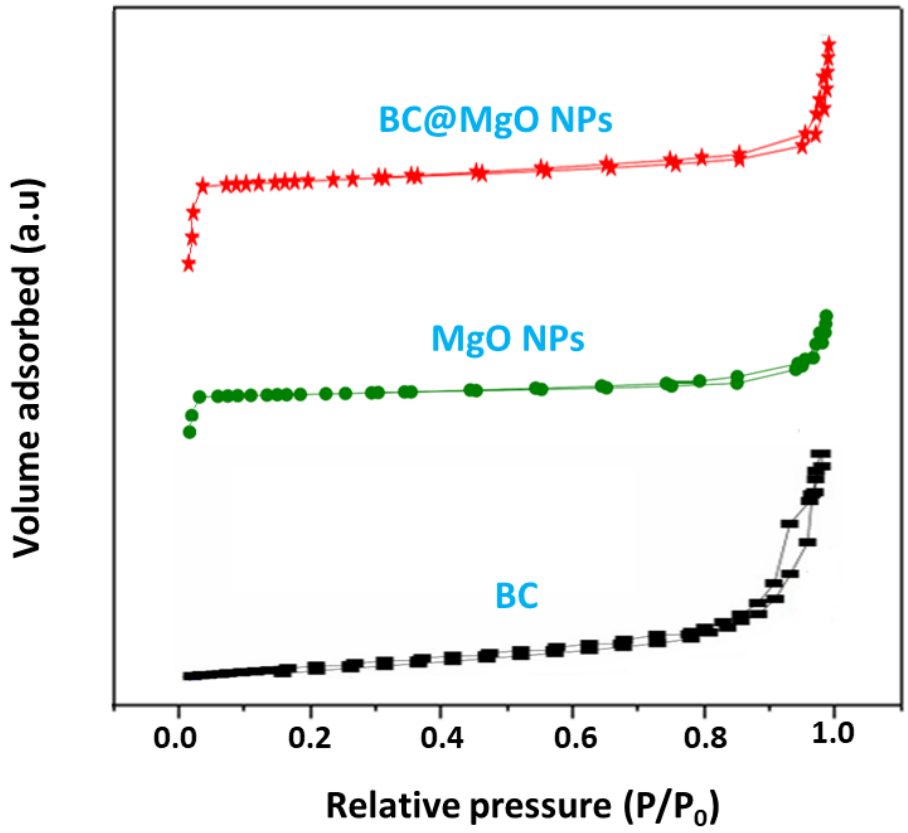

Fig.2. Curves of N_2 adsorption/desorption isotherms of BC, MgO NPs, and BC@MgO NPs.

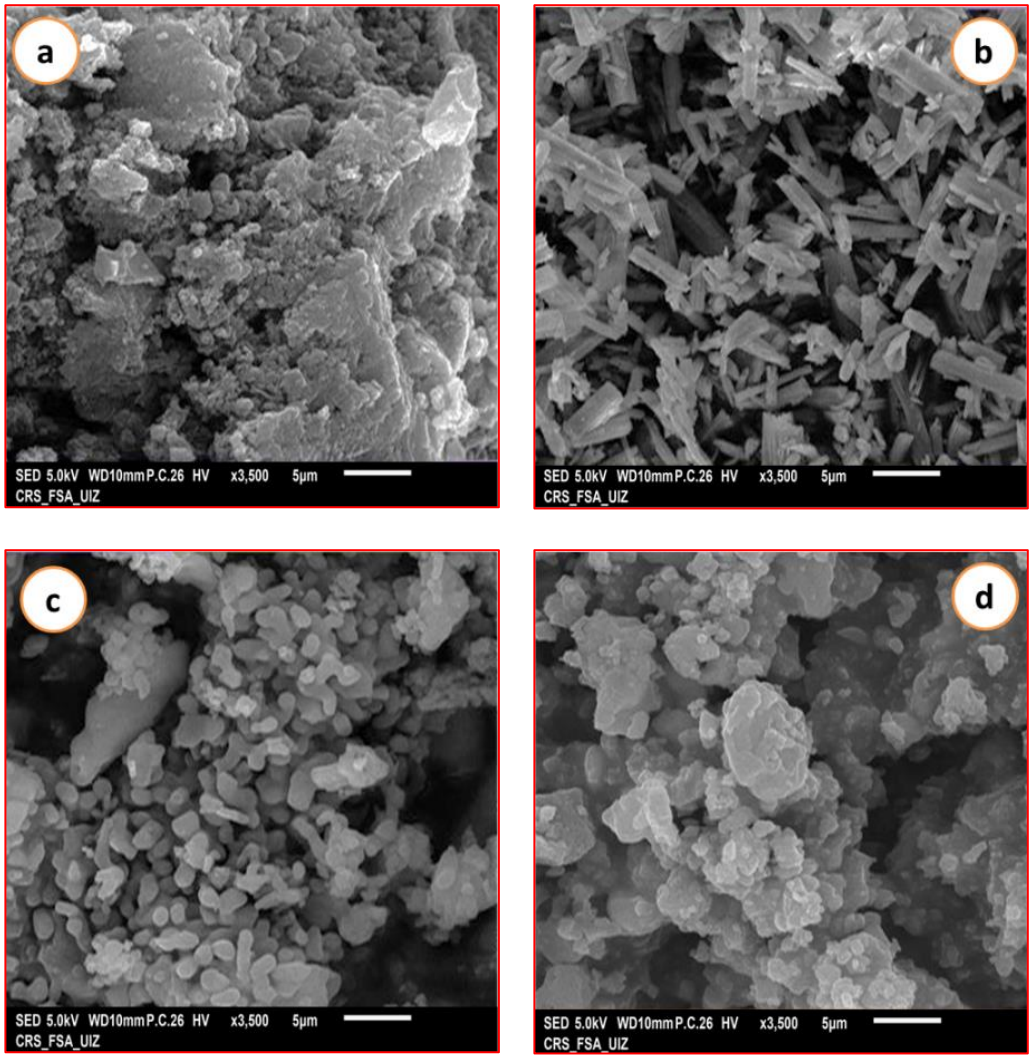

Fig.3. SEM images of BC (**a**) MgO NPs (**b**), BC@MgO NPs (**c**), and TZ-BC@MgO NPs (**d**).

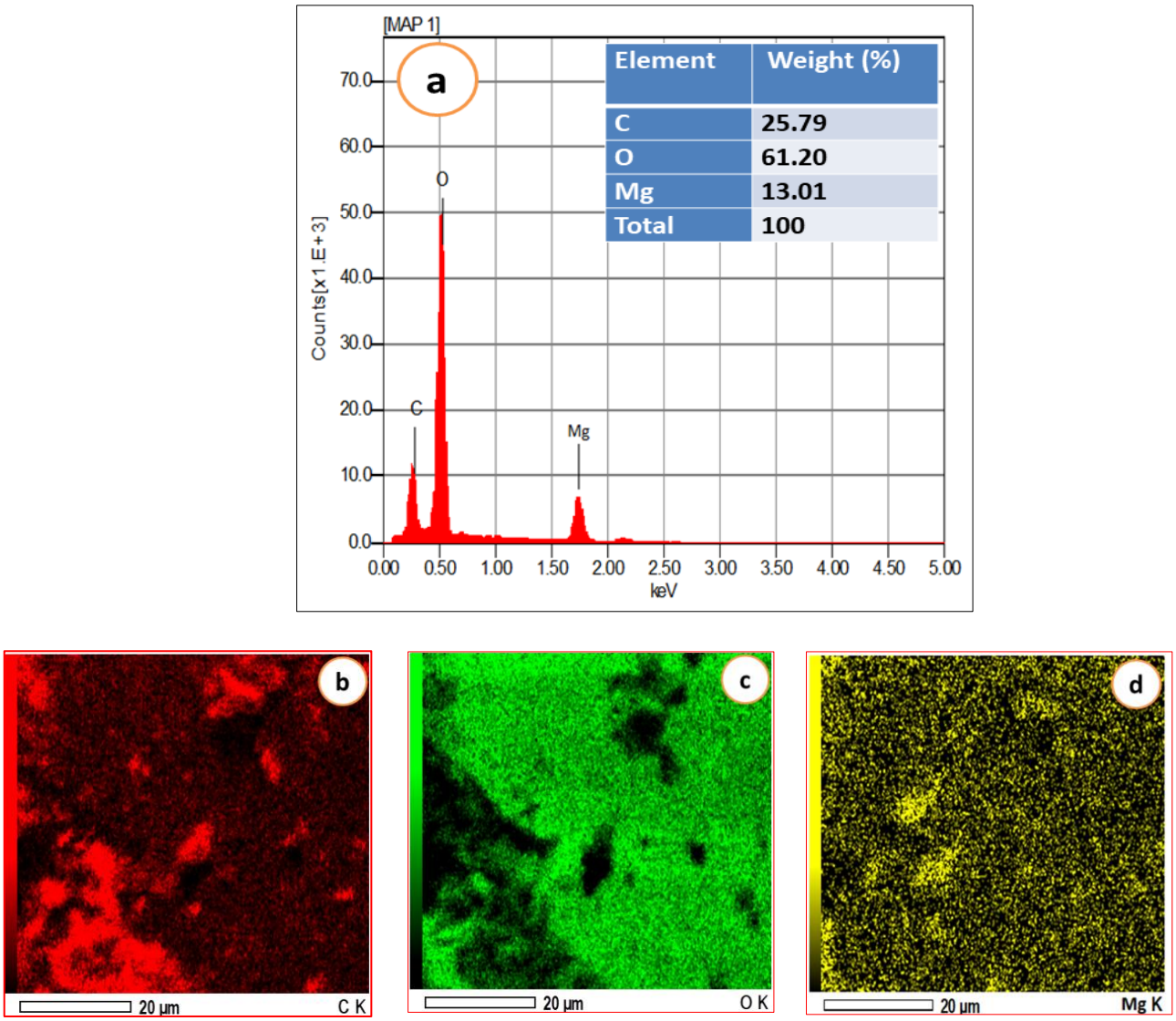

Fig.4. EDX elemental analysis of BC@MgO NPS (**a**), elemental mapping images of carbon (**b**), oxygen (**c**), and magnesium (**d**) for BC@MgO NPs.

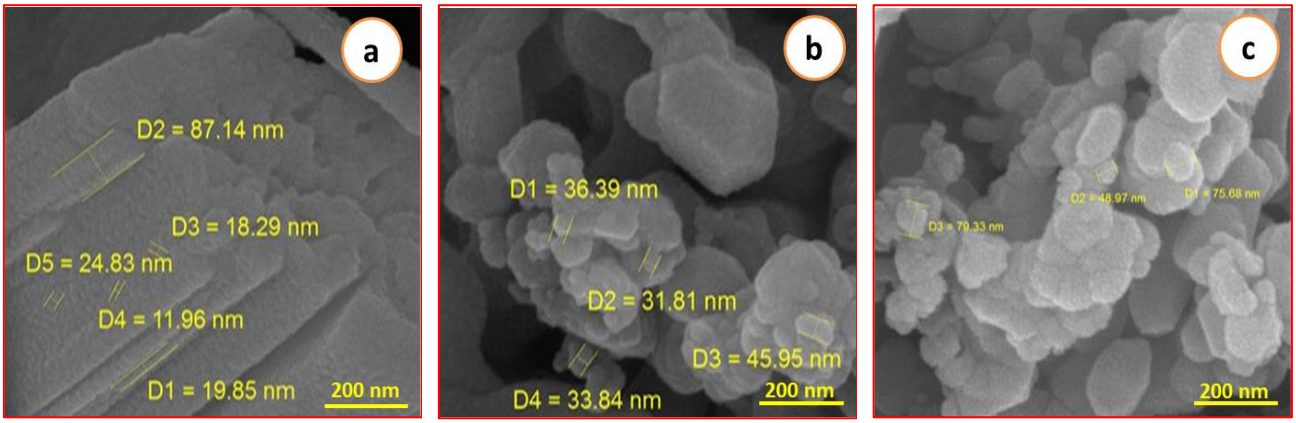

Fig.5. TEM images of MgO NPs (**a**), BC@MgO NPs (**b**), and TZ-BC@MgO NPs (**c**).

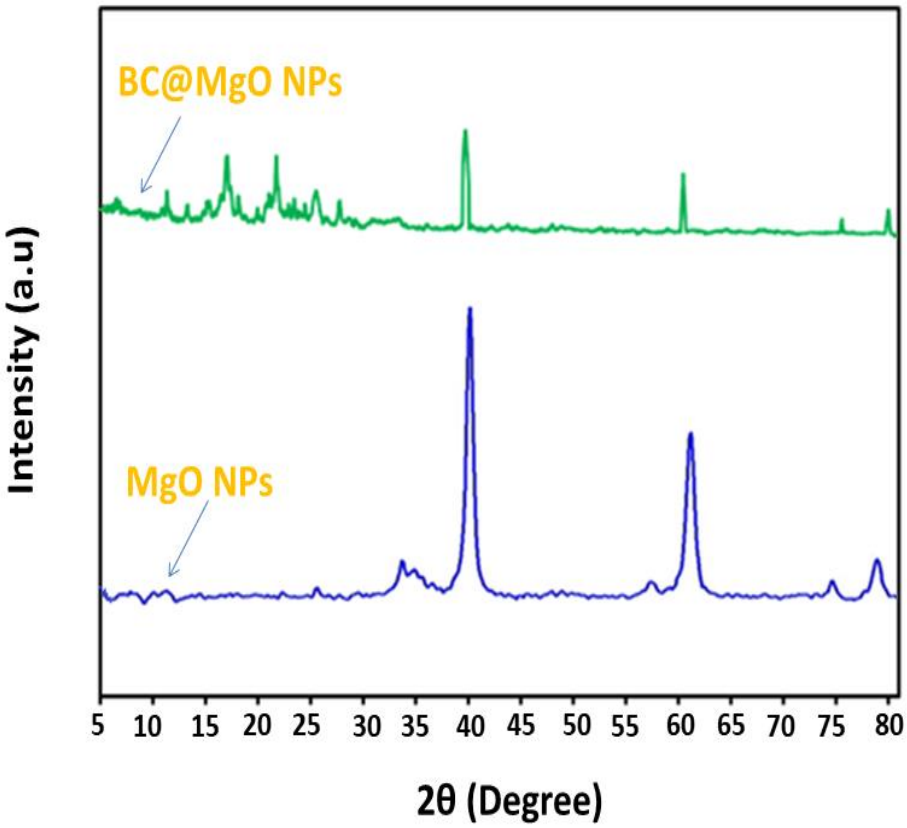

Fig.6. XRD spectra of MgO NPs and BC@MgO NPs.

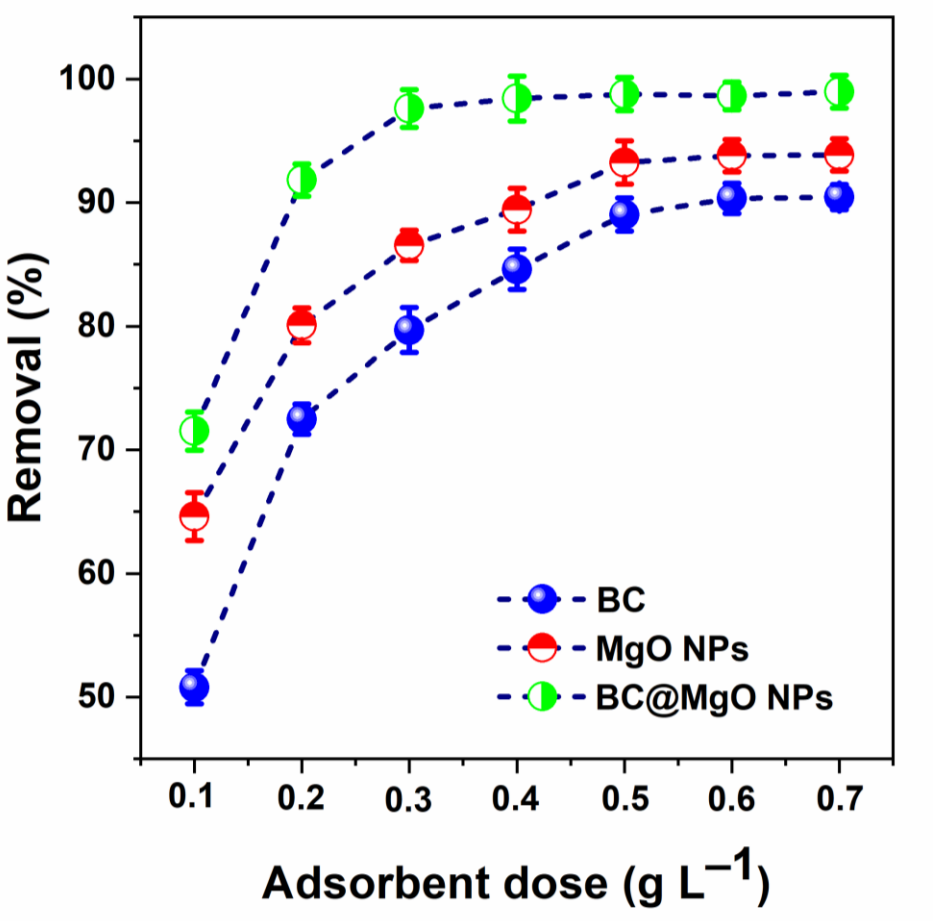

Fig.7. Influence of adsorbent dose on TZ adsorption.

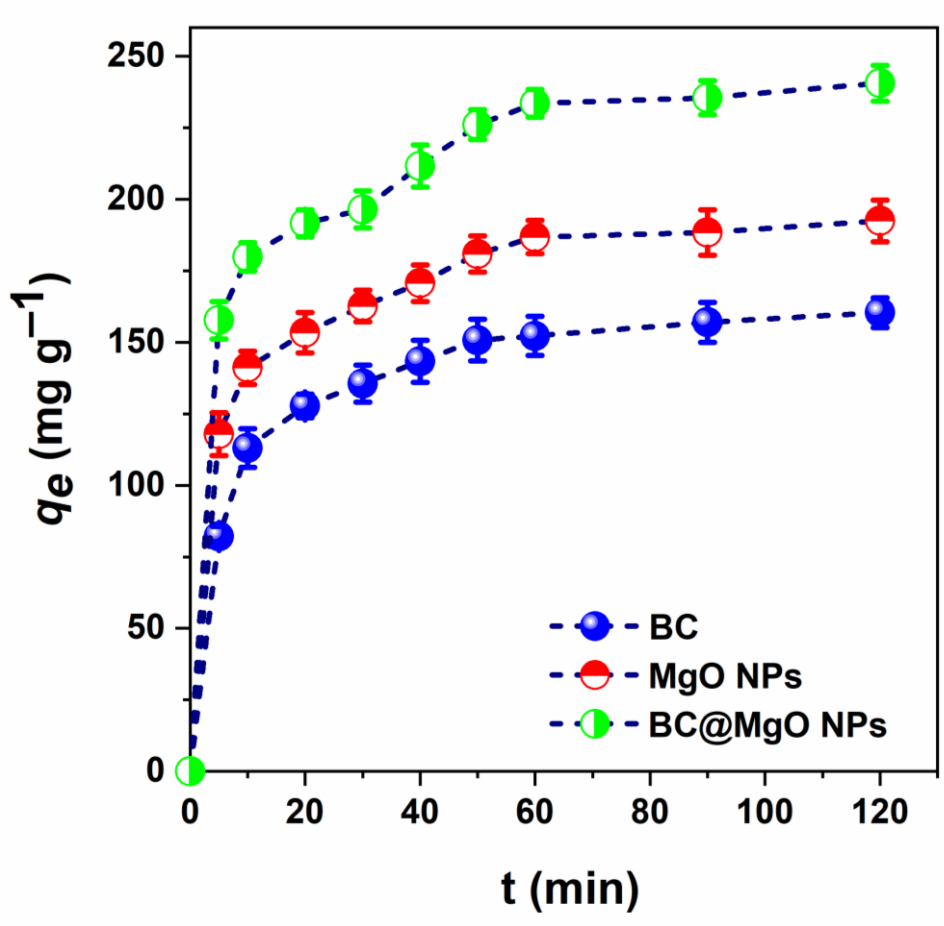

Fig.8. Effect of contact time on TZ adsorption.

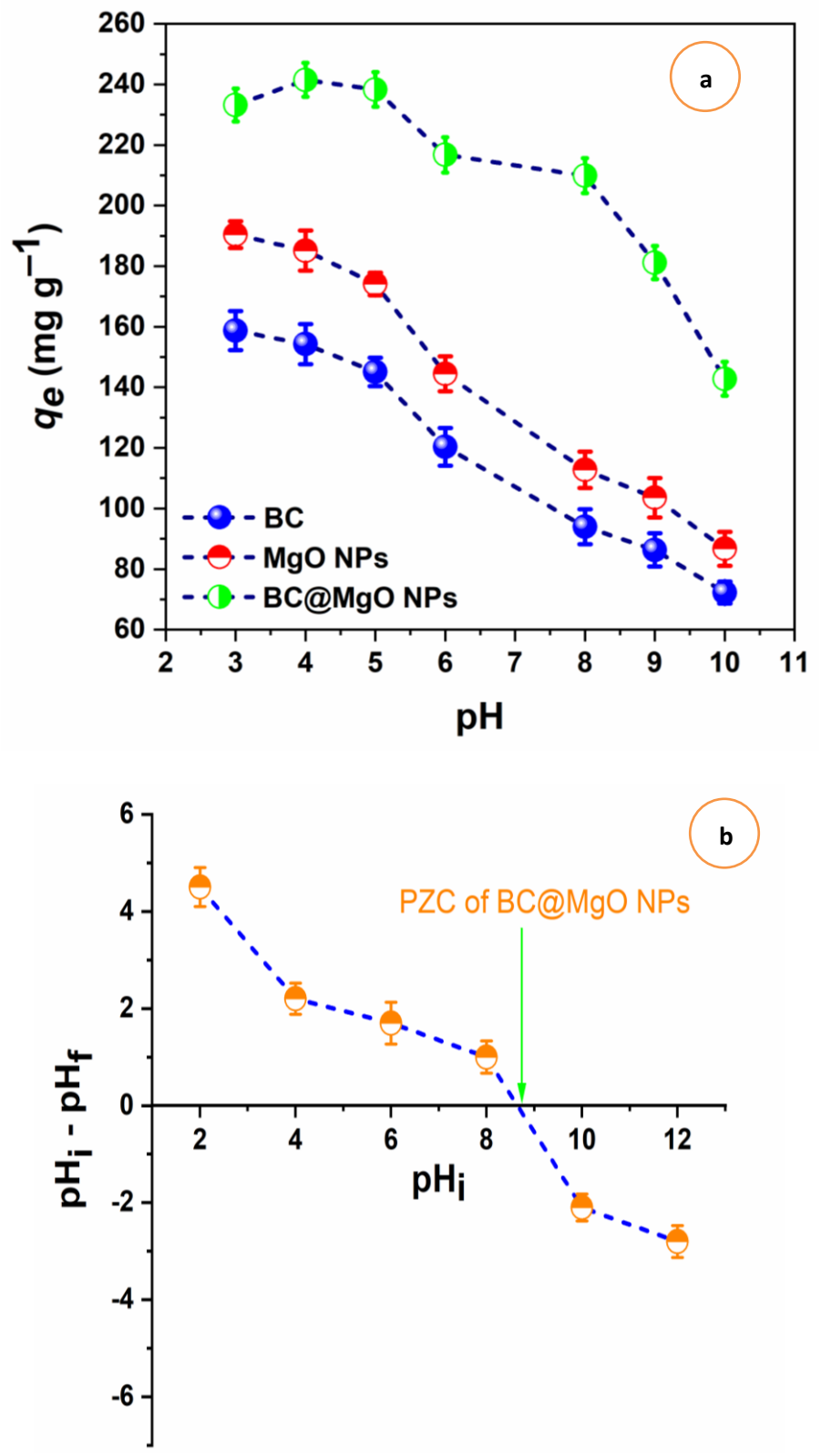

Fig.9. Quantity adsorbed as a function of pH (**a**) and PZC of BC@MgO NPs (**b**).

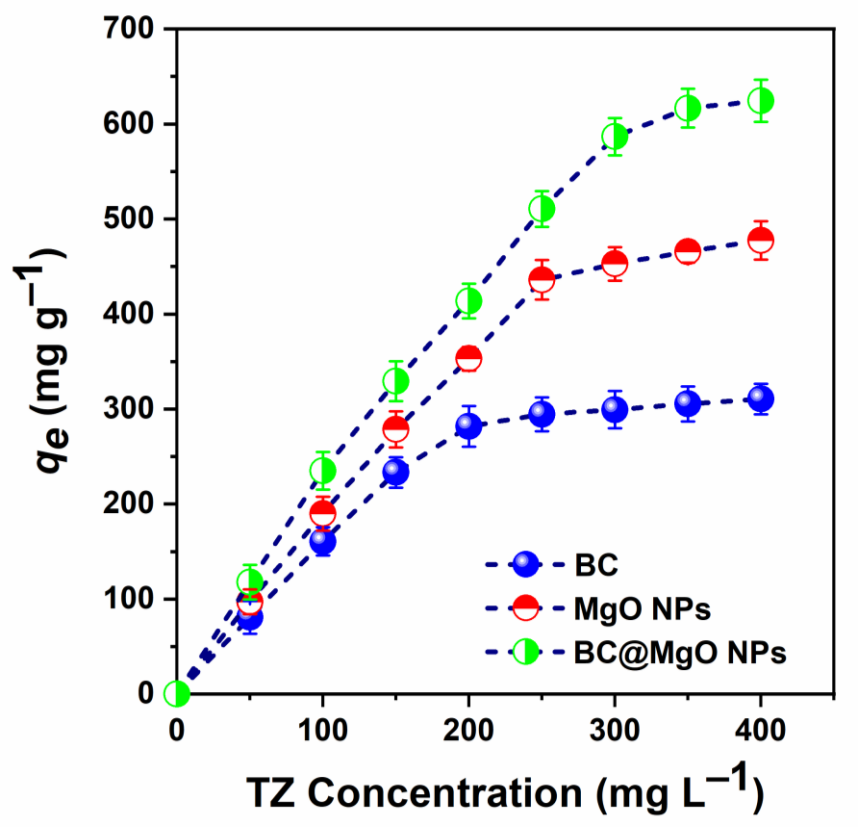

Fig.10. Effect of TZ concentration on TZ adsorption.

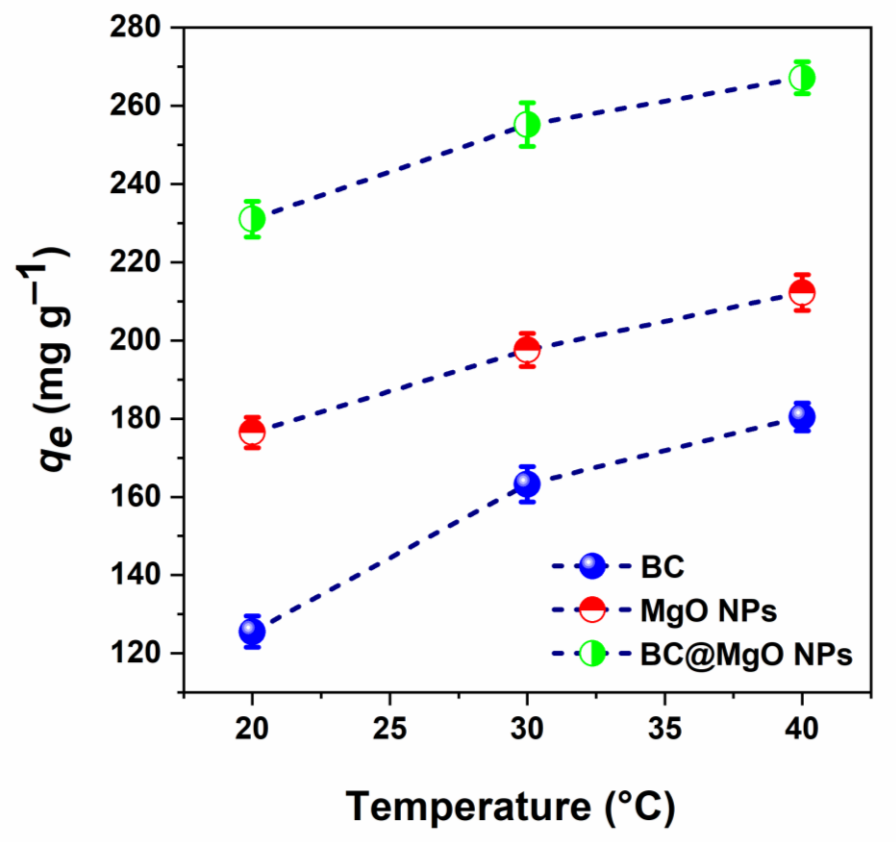

Fig.11. Effect of temperature on TZ adsorption.

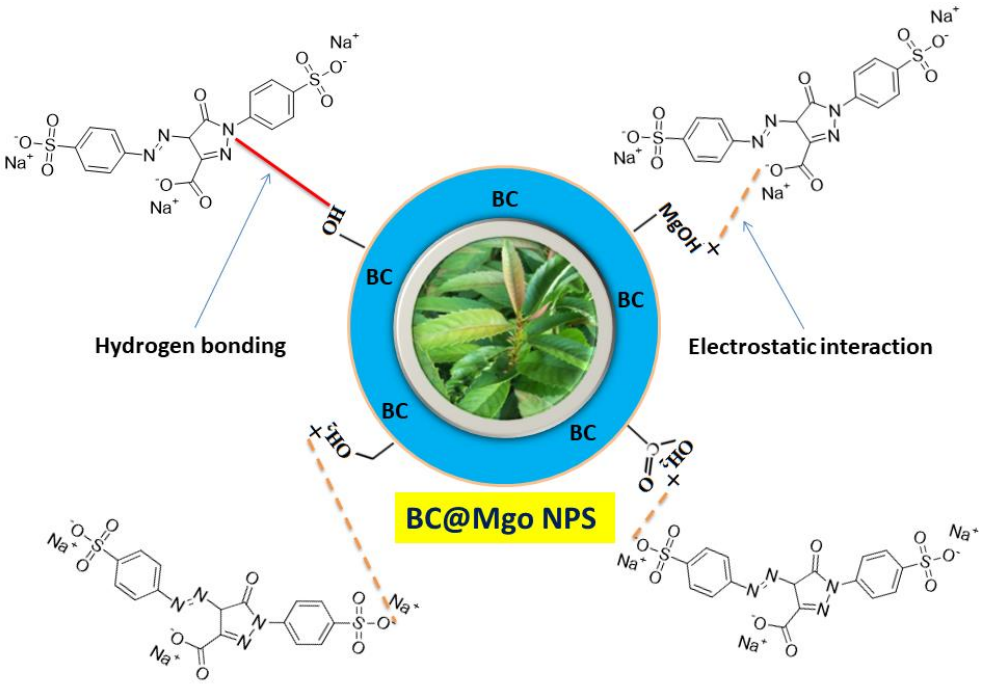

Fig.12. Proposed adsorption mechanism of TZ on BC@MgO NPs.

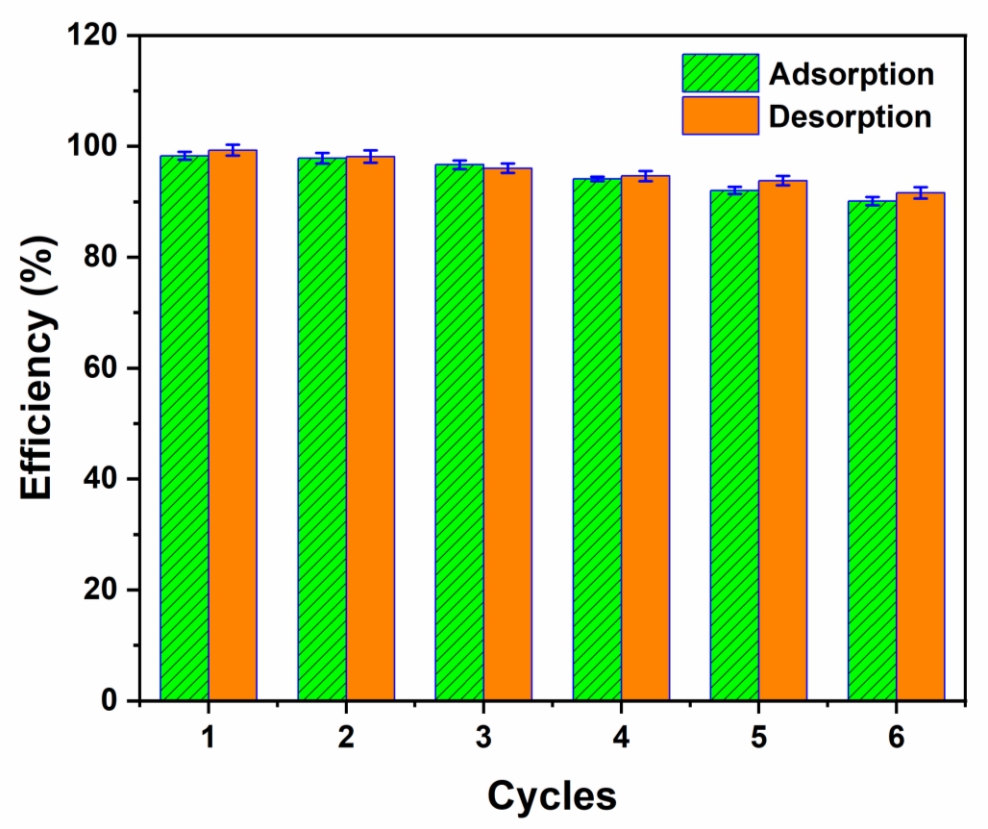

Fig.13. Regeneration of BC@MgO NPs in the removal of TZ.

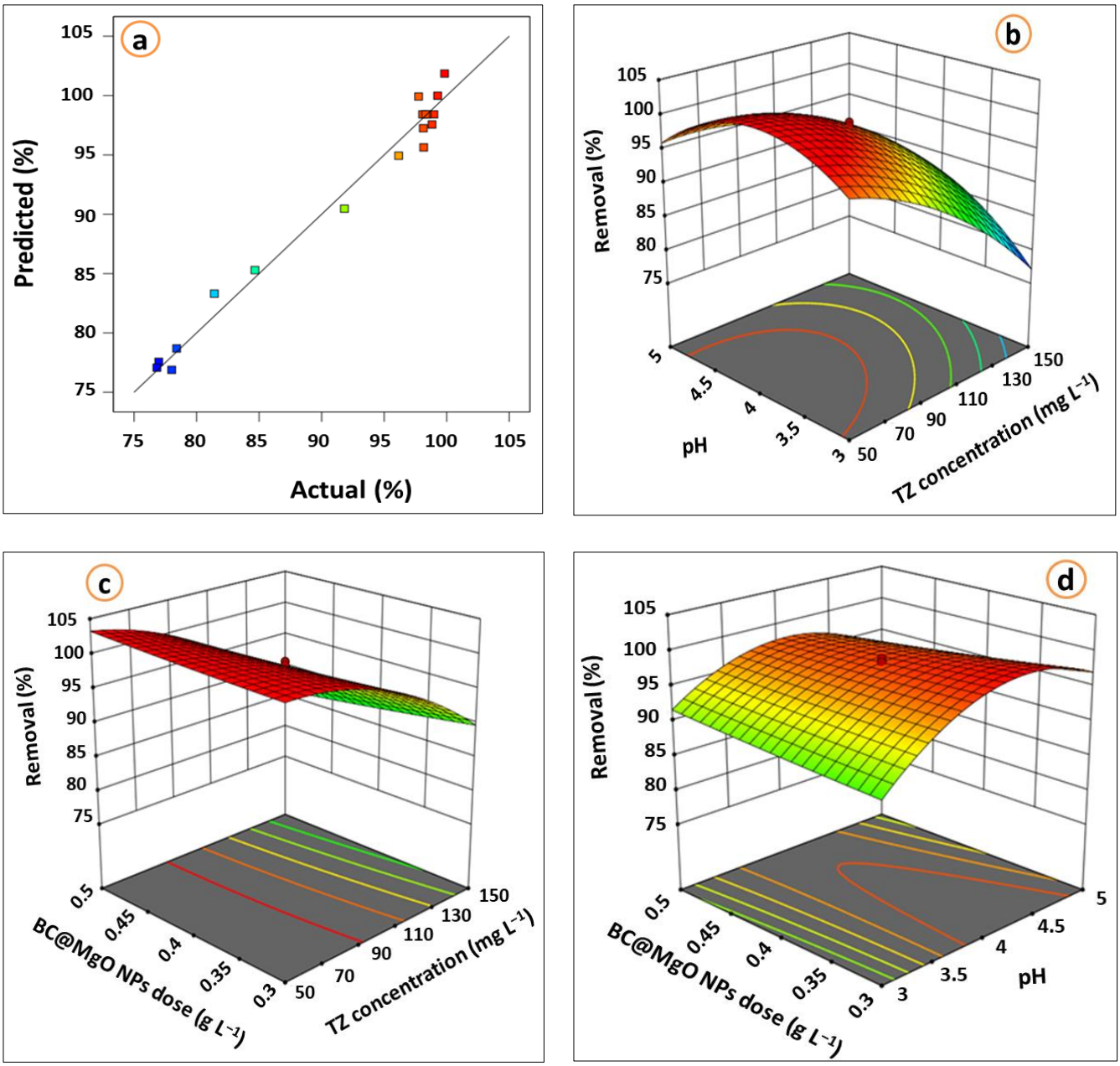

Fig.14. Actual versus predicted response (**a**), 3D surface response curves: initial TZ concentration with pH (**b**), BC@MgO NPs dose with initial TZ concentration (**c**), BC@MgO NPs dose, and with pH (**d**).

List of Tables

Table 1. Box–Behnken design data for TZ removal by BC@MgO NPs.

Variables			**Codes**		
			-1	0	1
X_1:TZ concentration (mg L^{-1})			50	100	150
X_2: pH			3	4	5
X_3: BC@MgO NPs dose (g L^{-1})			0.3	0.4	0.5
Run	**X_1 (mg L^{-1})**	**X_2**	**X_3 (g L^{-1})**		**R (%)**
1	50	3	0.3		98.16
2	150	3	0.3		76.98
3	50	5	0.3		98.13
4	150	5	0.3		91.82
5	50	3	0.5		98.28
6	150	3	0.5		76.83
7	50	5	0.5		96.16
8	150	5	0.5		81.42
9	50	4	0.4		99.51
10	150	4	0.4		78.01
11	100	3	0.4		88.41
12	100	5	0.4		84.67
13	100	4	0.3		97.75
14	100	4	0.5		98.56
15	100	4	0.4		98.48
16	100	4	0.4		98.44
17	100	4	0.4		98.08
18	100	4	0.4		98.32

Table 2. Kinetic parameters for TZ adsorption toward BC, MgO NPs, and BC@MgO NPs.

Model	**Parameter**	**Adsorbent**		
		BC	**MgO NPs**	**BC@MgO NPs**
	$q_{e,exp}$ (mg g^{-1})	160.37	192.44	240.55
	$q_{e,cal}$ (mg g^{-1})	136.74	109.54	97.16
PFO	K_{PFO} (min^{-1})	0.0066	0.0101	0.0354
	R^2	0.7965	0.8752	0.8951
	$q_{e,cal}$ (mg g^{-1})	163.93	196.07	243.90
PSO	K_{PSO} (g mg^{-1} min^{-1})	0.0010	0.0009	0.0008
	R^2	0.9996	0.9990	0.9981
	α_e (mg g^{-1} min^{-1})	10725	13561	16461
Elovich	β_e (g mg^{-1})	0.4687	0.3911	0.3528
	R^2	0.9487	0.9145	0.9023

Table 3. Isotherm parameters for TZ adsorption toward BC, MgO NPs, and BC@MgO NPs.

Model	**Parameter**	Adsorbent		
		BC	**MgO NPs**	**BC@MgO NPs**
	Q_m (mg g^{-1})	313.74	480.76	643.50
Langmuir	K_L (L mg^{-1})	0.1280	0.1053	0.0658
	R^2	0.9998	0.9993	0.9935
	K_F (mg g^{-1})	96.6987	95.0930	94.2357
Freundlich	N	3.4977	2.6136	2.4177
	R^2	0.8079	0.9057	0.9419
	K_T (L g^{-1})	2.1598	1.4636	1.2343
Temkin	B	77.13	105.14	153.81
	R^2	0.9055	0.9591	0.9724

Table 4. Comparison of Q_m of BC@MgO NPs with other materials for TZ removal.

Adsorbent	**Q_m (mg g^{-1})**	**Reference**
Mixed-waste activated carbon	74.90	(Habila et al., 2014)
Zn_2Al/Cl-Layered double hydroxide	282.48	(Ouassif et al., 2020)
$NiFe_2O_4$ nanoparticles	107.10	(Zandipak and Sobhanardakani, 2016)
Chitosan/polyaniline	580.00	(Sahnoun and Boutahala, 2018)
Polypyrrole/$SrFe_{12}O_{19}$/graphene oxide	123.50	(Ebrahimpoor et al., 2021)
Schiff base network-1/ Montomorillonite	602.70	(Khataei et al., 2020)
Cobalt hydroxide nanosorbent	142.3	(Bagtash and Zolgharnein, 2018)
BC	313.74	This work
MgO NPs	480.76	This work
BC@MgO NPs	643.50	This work

Table 5. Thermodynamic parameters for TZ adsorption toward BC, MgO NPs, and BC@MgO NPs.

Adsorbent	***T* (K)**	***ΔG°*** (kJ mol^{-1})	***ΔH°*** (kJ mol^{-1})	***ΔS°*** (J mol^{-1} K^{-1})
	293	–10.5405		
BC	303	–11.1389	33.4589	103.7852
	313	–11.8743		
	293	-7.1745		
MgO NPs	303	-7.4194	42.7452	115.8934
	313	-7.6642		
	293	–6.6971		
BC@MgO NPs	303	–6.9257	87.9652	147.7864
	313	–7.1543		

Table 6. ANOVA data for a designed model of TZ dye adsorption onto BC@MgO NPs.

Source	**Sun Squares**	**df**	**Mean Square**	**F-value**	**p-value**
Model	1426.29	9	158.48	46.00	< 0.0001
X_1:TZ concentration	752.53	1	752.53	218.44	< 0.0001
X_2: pH	52.62	1	52.62	15.28	0.0045
X_3:BC@MgO NPs dose	6.73	1	6.73	1.95	0.1999
X_1X_2	63.73	1	63.73	18.50	0.0026
X_1X_3	11.76	1	11.76	3.41	0.1018
X_2X_3	22.24	1	22.24	6.46	0.0347
X_1^2	129.32	1	129.32	37.54	0.0003
X_2^2	426.49	1	426.49	123.80	< 0.0001
X_3^2	0.1684	1	0.1684	0.0489	0.8306
Residual	27.56	8	3.45		
Lack of Fit	27.13	5	5.43	37.44	0.0066
Pure Error	0.4347	3	0.1449		
Core total	1453.85	17			
Model statistics	R^2	Adjusted R^2	Predicted R^2	Adequate precision	
	0.9810	0.9597	0.8508	18.0480	